PEER REVIEWED

Mechanical and Fatigue Properties of Diamond-Reinforced Cu and Al Metal Matrix Composites Prepared by Cold Spray

O. Kovarik[1] · J. Cizek[2] · S. Yin[3] · R. Lupoi[3] · M. Janovska[4] · J. Cech[1] ·
J. Capek[1] · J. Siegl[1] · T. Chraska[2]

Abstract Diamond-reinforced metal matrix composites (DMMC) prepared by cold spray are emerging materials simultaneously featuring outstanding thermal conductivity and wear resistance. In our paper, their mechanical and fatigue properties relevant to perspective engineering applications were investigated using miniature bending specimens. Two different diamond mass concentrations (20 and 50%) embedded in two metal matrices (Al—lighter than diamond, Cu—heavier than diamond) were compared with the respective cold-sprayed pure metals, as well as bulk Al and Cu references. The pure Al, Cu coatings showed properties typical for cold spray deposits, i.e., decreased elastic moduli (50 GPa for Al, 80 GPa for Cu), limited ductility ($< 1 \times 10^{-3}$) and low fracture toughness (3.8 MPa·m$^{0.5}$ for Al, 5.6 MPa·m$^{0.5}$ for Cu) when compared to the bulks. Significantly improved properties (strain at fracture, ultimate strength, fatigue crack growth resistance, fracture toughness) were then observed for the produced DMMC. The improvement can be explained by a combination of two factors: changes in the properties of the metallic matrix triggered by the reinforcement particles peening effect and stress redistribution due to the particles presence.

Keywords cold spray · properties · properties, fatigue · properties, fracture · processing diamond metal matrix composites, mechanical properties

✉ O. Kovarik
ondrej.kovarik@fjfi.cvut.cz

1. Faculty of Nuclear Sciences and Physical Engineering, Czech Technical University in Prague, Prague, Czech Republic

2. Institute of Plasma Physics of the Czech Academy of Sciences, Prague, Czech Republic

3. Trinity College Dublin, The University of Dublin, Dublin, Ireland

4. Institute of Thermomechanics of the Czech Academy of Sciences, Prague, Czech Republic

Introduction

Diamond-based metal matrix composites (DMMC) combine load-bearing properties of a ductile metal matrix with the high hardness and thermal conductivity of the diamond reinforcement. It is therefore not surprising that DMMC and their properties have been extensively studied, including different manufacturing processes or the effect of the diamond content. For example, the review (Ref 1) shows that Cu–diamond composite with 50% diamond by volume can reach the thermal conductivity of 800 W/(m·K). According to the Maxwell model, this is twice as much as pure Cu. Another example is the Cu-based DMMC studied in (Ref 2), which showed pin-on-disk wear resistances ranging from 1.1×10^{-6} to 1.4×10^{-6} mm^2/N. Again, compared to pure copper (wear rate of 3×10^{-3} mm^2/N), this is an improvement by three orders of magnitude. Needless to say, these attractive properties predetermine DMMC use, e.g., for superior thermally conducting abrasives (i.e., materials that can absorb the friction-generated heat easily) or electrical contacts. For such applications, good mechanical and fracture properties are required. For DMMC, these are defined by the quality

of the matrix and the reinforcement particles, as well as the matrix–particle interfaces.

There are several DMMC production routes, including sintering techniques (Ref 3), pressure infiltration (Ref 4) and spray techniques (Ref 5). The former two methods are widely used, but require high-temperature processing, which may lead to high residual thermal stress development and also require additional care to avoid diamond graphitization (Ref 6). Typically, around 600°C and 800–1000°C are necessary for Al and Cu sintering, and even higher temperatures are needed for the infiltration-based techniques which require a full melting of the matrix material. The typical properties of DMMC prepared by these standard methods are reviewed in (Ref 7). In that paper, the fracture toughness and ultimate strength of particle-reinforced aluminum alloys were observed to increase together with the particle content (while, at the same time, the ductility decreased). Generally, the sintering and infiltration methods can generate high-quality DMMC, but are somehow limited when it comes to joining the DMMC with an underlying support material. Unfortunately, this is a critical quality for a number of targeted applications, as a good adherence to the support material would enable a cost-effective solution of covering only the abrasively loaded area with the relatively expensive DMMC. This opens up the potential for the spray techniques. From the available coating methods, oxy-acetylene and HVOF (Ref 5), as well as cold spray (CS) (see (Ref 8) and (Ref 2)) were studied. Cold spray can deposit DMMC without exposing the materials to high temperatures, thereby avoiding the graphitization as indicated in our previous study (Ref 2), tensile residual stresses development (Ref 9) and limiting several other drawbacks inherently associated with the high-temperature methods. The difficulty here lies in the fact that diamond-based coatings are not easily deposited due to the low deposition efficiency of the brittle diamond particles (Ref 8). However, recent studies showed that cladding of the individual diamond particles resolves this problem and also prevents the diamond phase fragmentation (see (Ref 2) and (Ref 10)), thereby enabling production of thick, high diamond content coatings. At the same time, the observed strength and density of the cold-sprayed DMMC are relatively high (Ref 10), suggesting good engineering properties of the material.

The cold spray technique differs significantly from the other discussed manufacturing routes, introducing a significant plastic deformation to the matrix material and putting the reinforcement particles under high dynamical loading upon their impact. As a consequence, the reinforcement mechanisms known in conventional MMC (Ref 11), i.e., micro-mechanical matrix strengthening or stress redistribution into the reinforcement particles, may be

limited for the CS route. At the same time, other mechanisms not commonly encountered may be active, such as the peening effect of diamond reinforcement.

Typically, the matrix strengthening observed in conventionally manufactured MMCs is caused by a formation of substructure, grain refinement or dislocation density increase. These mechanisms are triggered by dislocation activity driven by externally imposed stresses and amplified by the presence of reinforcement particles (Ref 11). In the heavily deformed cold spray materials though, the dislocation mobility is already limited by splat interfaces with high dislocation density formed by plastic deformation at the impact. Therefore, further strengthening of a cold-sprayed matrix by the described mechanisms will be limited (with the exception of materials that anneal upon their deposition, as commonly observed for, e.g., Al deposits). In our study, the strengthening mechanisms are not studied separately and are considered to be one of the possible causes of matrix property changes.

Aside from stimulating the strengthening micro-mechanisms, the reinforcement particles can also influence the DMMC stress–strain behavior by carrying a significant part of the imposed load due to their high stiffness. This effect is well described by the Eschelby equivalent inclusion approach-based methods (Ref 12) or by FEM modeling using special element types (Ref 13). It is shown that when the reinforcement–matrix interface bond strength is sufficient, a significant strength enhancement can be achieved. In cold spray, the inter-splat bonding quality generally predetermines the material strength and ductility, as it generally represents the weakest part of the material. In an approximation, the inter-splat interface can be considered a combined metallurgical–geometrical joint of two highly deformed splat boundaries. Naturally, its strength will differ for the case when one of the splats is the reinforcement particle. Indeed, as already concluded in the previous work (Ref 10), the reinforcement–matrix interface represents a weak link in the cold-sprayed DMMC, a factor that will significantly limit the stress redistribution.

With the uncertainty about the mechanisms that govern the influence of the diamond phase in CS in mind, our paper tries to explore the relevant properties of the cold-sprayed DMMC. We studied the relation between the architecture of the composite deposits, their engineering properties and the associated failure mechanisms. Double-clad diamond particles were sprayed together with two metallic matrices: lighter and more compliant Al matrix, and heavier and stiffer Cu matrix. Al and Cu were selected owing to their high thermal conductivity and significantly different densities and stiffnesses. This approach enabled to observe the effect of the reinforcement-to-matrix density or stiffness ratio: higher stiffness or density of the reinforcement causes higher impact stresses and induces more

prominent matrix property changes around the impact position (Ref 14). Based on the results of (Ref 2) and with the intended grinding and cutting application in mind, two different diamond concentrations (20 and 50% by weight) were tested for each matrix, in order to study the effect of diamond content.

Characterization of basic stress–strain properties, fracture mechanics, as well as fatigue properties of the deposits was performed for all combinations of the matrix material and diamond concentration. All testing methods were performed on self-standing deposit material, therefore the effects of substrate material and substrate–deposit interface on tested properties were avoided. It was shown that the presence of diamond particles improves most of the investigated mechanical properties when compared to the corresponding cold-sprayed pure metals. To evaluate the effect of the individual mechanisms that form the properties of DMMC, the local matrix properties such as residual stress, hardness and modulus were investigated as well as failure mode of both the reinforcement particles and matrix. The results were compared with pure metal deposits sprayed with the same deposition system, as well as a high-pressure commercial one.

Materials and Methods

The feedstock powders consisted of a mechanical mixture of either Al ($-58 + 15$ μm, Valimet, USA) or Cu ($-38 + 15$ μm, Safina, Czech Republic) powders with a double-clad diamond powder. The cladded particles ($-53 + 45$ μm, PDA C50, Element-Six, Ireland) consisted of a diamond core, a thin Ni interlayer and a Cu shell. The total cladding-to-diamond weight ratio was approximately 1:1, corresponding to a combined cladding layer thickness of 2–5 μm. The densities of all materials are summarized in Table 1. Aside from the two pure metals used as a reference (denoted as Al100, Cu100), four composites containing 20 and 50 wt.% of the clad diamond particles in the feedstock powder were sprayed (denoted as Al80, Cu80, and Al50, Cu50). The coatings were deposited by an in-house developed cold spray system (Trinity College Dublin, Ireland). The system consists of a gas heater, powder feeder, CNC working platform for controlling the

substrate movement, de Laval nozzle and a computer control system. High-pressure He gas was used for spraying. The spray nozzle had a throat diameter and an exit diameter of 2 and 6 mm, respectively, with a total length of 210 mm. The used deposition parameters listed in Table 2 were reproduced from the previous study (Ref 2). Graphite-free coatings were obtained, as evidenced by x-ray analysis in that paper. At the same time, the deposition efficiency of the double-clad diamond particles was comparable with that of the pure Cu powder as indicated by EDX compositional analysis in (Ref 2). The deposition was performed on $60 \times 40 \times 3$ mm^3 aluminum alloy substrates and the coating thickness was around 5 mm. Another two pure metal deposits denoted as Al100[*] and Cu100[*] deposited by a high-pressure commercial system in our previous work (Ref 15) (ISS 5/11, OUT1 nozzle, nitrogen process gas; Impact Innovations, GmbH., Germany) were also tested in this paper to understand the obtained results in a broader context.

The coatings microstructure was studied in an electron channeling contrast mode (ECCI) using JEOL JSM-IT500HR (JEOL, Osaka, Japan) field emission SEM. The pure metal specimens were ground and polished by conventional metallography techniques, while the samples containing diamonds were polished using colloidal silica on hard napless cloth for 30 minutes, cleaning the specimen and the cloth every 5 minutes. The final polishing step was performed using colloidal silica vibratory polishing for 4 hours (Vibromet, Buehler, Lake Bluff, USA) to reveal fine microstructure details and enable electron channeling contrast imaging.

Density was measured using Archimedes method using ABT-A01 kit and ABT-NM analytical scale (Kern & Sohn GmbH, Balingen, Germany). Universal rectangular bar specimens were used for the measurement. Both open and closed porosity was considered when evaluating the measurements.

Hardness (H_{IT}) and elastic modulus (E_{IT}) of the matrix were measured by an instrumented indentation technique according to ISO 14577 standard. The tests were carried out using MHT microhardness tester (Anton Paar GmbH, Graz, Austria) equipped with Vickers diamond indenter. The indentation cycle consisted of loading to a maximum force, dwell and unloading, lasting for 30 s, 10 s and 30 s,

Table 1 Properties of the materials relevant to this study compiled from [39, 40] and [19]. The clad diamond density was calculated assuming a 1:1 diamond-to-cladding weight ratio

Material	ρ (kg/m^3)	E (GPa)	R_m (MPa)	A (%)	K_{IC} (MPa·m$^{0.5}$)
Diamond	3510	1050	.		4.7–14
Clad diamond	5000				
Ni	8902	210	3610–660	25–45	194.1
Al	2700	69	55–160	9–55	.
Cu	8960	110	216–448	13-45	134.5

Table 2 Deposition parameters of the investigated cold-sprayed DMMC coatings and coatings Al100[*] and Cu100[*] sprayed by a high-pressure commercial system

Deposit	Gas pressure (MPa)	Gas temperature (°C)	Standoff distance (mm)	Torch traversal speed (mm/s)
Al-based coatings	3.0	400	35	50
Cu-based coatings	3.0	600	35	50
Al100[*]	5.0	500	30	500
Cu100[*]	3.8	450	30	500

respectively. The maximum load-force was set to 0.5 N in order to keep the indent diagonal below 50 μm. The indents were typically placed into the largest reinforcement-free areas of the specimen to avoid indenter contact with a diamond particle. At the same time, the mean free path between the reinforcement was typically around 100 μm (see Fig. 3). Consequently, the ratio of the indent size to the mean free path limits the potential influence of reinforcement particles on the measured matrix indentation properties. At the same time, even the smallest indents with 25 μm diagonal allowed to measure across several splats, comprehending the effect of inter-splat interfaces. Ten indents were performed and statistically processed for each material. All hardness values that were prominent outliers were removed as the influence of hidden reinforcement particles was suspected.

The elastic constants of the deposits were determined by resonant ultrasound spectroscopy (RUS). RUS is a well-established technique for investigation of elastic properties of solids based on the inversion of natural frequencies of free elastic vibrations of small, simple-shaped specimens (Ref 16). Small prismatic samples (approximately $1 \times 1 \times 1$ mm^3) were cut from each deposit. A fully non-contact setup described in detail in (Ref 17) was used. The sample was placed in an evacuated chamber with low nitrogen pressure (20 mbar) which enabled precise temperature control (± 0.1 °C) of the measured sample. Vibrations of very small strain amplitude in the order 10^{-6} were excited at the bottom face of the sample by infrared Nd:YAG laser (Quantel ULTRA, nominal wavelength 1.064 μm, pulse duration 8 ns). The upper face of the sample was scanned by a scanning laser vibrometer (MSA-500) to obtain frequencies and modal shapes of individual resonant modes. Resonant spectra of the free vibrating samples were recorded in frequency range 0.1–1 MHz, which covered the first 40 resonant peaks. These resonant frequencies together with the velocities of longitudinal waves in direction perpendicular to sample faces were involved in an inverse procedure to determine the elastic constants. A transversely isotropic material symmetry described by five independent elastic coefficients (c_{11}, c_{12}, c_{13}, c_{33} and c_{44} in Voight's notation) was assumed. The

out-of-plane elastic modulus in spray direction E_S and in-plane modulus E_{LT} was calculated from c_{ij} using simple algebraic relations (see, e.g., (Ref 18)).

All mechanical testing of the deposits, i.e., stress–strain measurements, fatigue crack growth rate tests, as well as fracture toughness measurements used a unified rectangular specimen geometry of $3 \times 4 \times 32$ mm^3 described in (Ref 19). The specimens were cut from the coatings using electric discharge machining. In total, five specimens were cut for each combination of matrix and diamond concentration. This allowed test replication for fatigue crack growth rate tests and fracture toughness tests, while a single specimen was used for the stress–strain testing where the lowest variability was expected. The specimen orientation denoted as L-T (analogous nomenclature to ASTM E399 standard) shown in Fig. 1 was used. This means that the T direction defines the crack propagation direction for fatigue and fracture toughness specimens, as well as the load line direction for bending stress–strain and fracture toughness specimens. The crack plane was always perpendicular to the longitudinal direction L of the spray pattern.

The stress–strain properties in both tension and compression were obtained from bending tests following the method of Herbert (Ref 20) and the setup described in (Ref
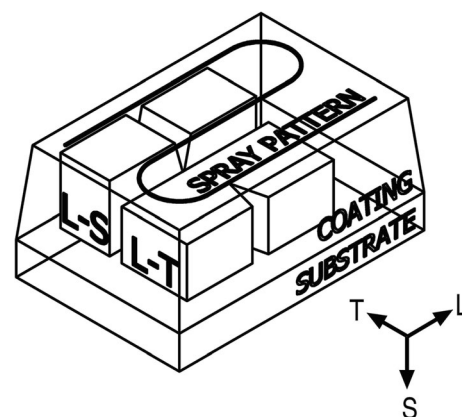

Fig. 1 Schematic drawing of the cold-sprayed deposit and defined orientations. Only specimens denoted L-T are investigated in this paper

15). The method uses a four-point bending fixture (4PB) with an outer span $L = 27$ mm and an inner span $l = L/2$. A crosshead speed of $u = 1 \times 10^{-6}$ m/s was used. The acting force was measured by a 1 kN-force transducer and the deformation at the upper and lower specimens' surfaces was recorded by digital image correlation (DIC) method using ncorr software (Ref 21). Blackfly 5-megapixel monochrome camera (FLIR Systems, Wilsonville, USA) equipped with in-line illuminated telecentric lens of $1\times$magnification (Edmund Optics, Barrington, NJ, USA) was used. The polished and etched specimen faces illuminated in a bright-field lighting mode provided good DIC texture and sufficient brightness. Incremental DIC was used to enable tracking of large deformation of the specimens. Circular subsets of 60-pixel diameter spaced at 5 pixels were used to compute the full displacement field of the specimen. The displacement field was then fitted with the displacement formula for pure bending, and the surface deformations ε_t, ε_c on the tension and compression sides were extracted. The corresponding stresses were computed by the following formula presented by Mayville and Finnie (Ref 22):

$$\sigma_\alpha = \frac{\mathrm{d}M(\varepsilon_t + \varepsilon_c) + 2M(\mathrm{d}\varepsilon_t + \mathrm{d}\varepsilon_c)}{bh^2\mathrm{d}\varepsilon_\alpha} \qquad \text{(Eq 1)}$$

where M is applied bending moment, b and h represent specimen thickness and width, and the suffix α stands for either c (for compression stress) or t (for tensile stress). The letter d is a differential operator and the numerical differentiation was performed using a four-point central difference formula. Apart from the tension and compression stress–strain curves $\sigma_t(\varepsilon_t)$ and $\sigma_c(\varepsilon_c)$ the standard bending stress–strain curve $\sigma(\varepsilon)$ assuming equal behavior in tension and compression ($\varepsilon_t = \varepsilon_c$) was also computed to be used for the evaluation of standard bending modulus E.

The fatigue crack growth rate measurement was based on ASTM E647 standard. Resonance technique was used to excite the specimen vibration at stress ratio $R \sim$ -1 and loading frequency in the range 120–200 Hz. The specimens were loaded in pure bending and the actual crack length was obtained using a differential compliance method. The details of the technique are given in (Ref 23). A straight notch of approximately 0.5 mm length was pre-cut to the specimens using a low-speed diamond saw. The experiment was performed in a rate-control mode, where the crack growth rate da/dN is prescribed as a function of crack length a and the load is adjusted by the control loop accordingly. That said, the nominal load varies throughout the experiment, typically ranging from 20 MPa for pure Al to 50 MPa for Cu-based DMMC. The crack was first grown to a crack length $a = 1.1$ mm at a crack growth rate decreasing from da/d$N \sim 10^{-9}$ m to da/d$N \sim 5 \times 10^{-11}$ m/cycle. The da/dN vs. K curve was then

measured with da/dN increasing exponentially from da/d$N \sim 5 \times 10^{-11}$ m/cycle to da/d$N \sim 1 \times 10^{-6}$ m/cycle.

The fracture toughness measurement on fatigue pre-cracked specimens followed the ASTM E1820 standard. The pre-cracking was performed at a crack growth rate of da/d$N \sim 10^{-9}$ m. The crack length and crack opening displacement (COD) was evaluated from the displacement field obtained by digital image correlation (DIC) by a method described in (Ref 15). The DIC approach further simplifies the COD measurement and makes it more robust compared to video-extensometer-based measurement used in (Ref 24). Using the DIC data to directly evaluate the J-integral by a method similar to (Ref 25) and (Ref 26) would be even simpler. However, this approach was unsuccessful in our study due to the local out-of-plane movement of the specimen surface near the crack tip that would require a 3D DIC system. The detailed description of the used fracture toughness measurement can be found in (Ref 15). Note that the other DIC-based measurements in this paper were performed at significantly lower specimen deformation, and a significantly smaller effect of out-of-plane displacements could therefore be expected. The critical value J_{IC} corresponding to J-integral at the onset of a stable crack growth was estimated from the R-curves describing the dependence of J-integral on crack extension Δa from fatigue pre-crack. The J-integral was converted to the fracture toughness using the plane stress formula $K_{IC} = \sqrt{EJ_{IC}}$.

Fractography was performed in both secondary electron and backscattered electron modes using JSM5500 field emission SEM (JEOL, Osaka, Japan). In order to investigate the failure mode of reinforcement particles, several pairs of backscattered SEM micrographs corresponding to opposing fracture surfaces were compared. For each of the used loading modes, i.e., near-threshold fatigue, Paris regime and final static fracture, three areas were observed. The images were manually aligned and the occurrence of reinforcement particles on the opposing fracture faces was analyzed based on their contrast. Over 2000 reinforcement particles were analyzed in total.

The *X'Pert PRO MPD* (Malvern Panalytical, Malvern, UK) diffractometer was used to measure the Al, Cu matrix strain in the L-direction (Fig. 1) for the pure metal deposits as well as the DMMC variants. The measurement was performed on finely polished surfaces of the self-standing universal specimens using Cr and Mn radiation with the average effective penetration depths 5–11 μm and 3–5 μm, respectively. Diffraction angles $2\theta^{hkl}$ were taken as a center of gravity of the {311} diffraction doublet. To determine residual stresses, the $\sin^2\psi$ method and x-ray elastic constants $\frac{1}{2}s_2 = 19.05$ TPa^{-1}, $s_1 = -4.89$ TPa^{-1} and $\frac{1}{2}s_2 = 11.74$ TPa^{-1}, $s_1 = -3.12$ TPa^{-1} were used for the

Al and the Cu phase, respectively. The values of $\sin^2\psi$ corresponding to positive and negative values of angles ψ were 0, 0.15, 0.3, 0.45, 0.6. Pinholes of 4×0.3 mm^2 in size determining the irradiated area were used. A rough estimation of the coherently diffracting domain size was determined from the {311} diffraction peak for $\psi = 0°$ tilt using the single-line Voigt function method, i.e., using the Scherrer equation.

Results and Discussion

Microstructure

The microstructure of deposits predetermines their mechanical and fatigue properties. The pseudo-3D microstructure of the Al, Cu pure metal coatings is presented in Fig. 2. The inter-splat pores (dark lines or areas) of the investigated Al100 deposit clearly show prevailing orientation in the L-T plane (i.e., perpendicular to spray direction). The high-pressure reference specimens Al100[*] and Cu100[*] show very limited porosity. The diamond distribution in the produced DMMC deposits is shown in Fig. 3. The diamond phase is distributed evenly and the content follows the feedstock trend. A more detailed microstructure of the matrix phase in all deposits is presented in Fig. 4. Both Al- and Cu-based deposits show a typical microstructure of cold-sprayed coatings, i.e., individual splats partially separated by inter-splat interfaces. These are represented by dark lines, while the individual grains inside the individual splats are defined by distinctive shades of gray, reflecting the grain orientation. Two grain size ranges were found in the matrix. The original coarse-grained feedstock microstructure was more or less preserved in each splat interior. Contrary to this, smaller, highly deformed grains were located along the inter-splat interfaces. The localized deformation of cold-sprayed splat interfaces is a well-known phenomenon that was modeled by several authors and experimentally detected with FIB-DIC strain mapping recently (Ref 27). In that study, the authors have shown that a cold-sprayed particle deforms plastically in the contact area due to inertia forces at impact, while the particle core deforms elastically. The rapid plastic deformation of the particle periphery can invoke a dynamic recrystallization by a mechanism described in (Ref 28). The size of a recrystallized grain will decrease with increasing impact pressure, which in turn depends on the particle density, stiffness and impact velocity. For a particular material, the dynamically recrystallized grain size may therefore indicate the energy available at the point of impact and thus the impact intensity. Unfortunately, the performed SEM analyses were not able to quantify the representative grain size distributions, mostly because of the high deformation of the observed grains. Some of the interfacial grains in our materials, especially in the Al-based deposits, have an equiaxial shape, suggesting a temperature-induced recovery and grain growth processes in the heavily deformed areas. According to the literature, the necessary recrystallization temperature is in the range 200–300°C for Al (Ref 29) and 250–350°C for Cu (Ref 30). Thus, the above processes may indeed readily take place, mainly in the Al-based matrix. In the Cu-based deposits, the fine grains at particle interfaces are mostly highly deformed, with common occurrence of twinning or deformation of the larger grains, indicating high stresses experienced by the copper matrix during its deposition. Twinning is indicated by a sharp change of ECCI contrast between areas corresponding to two different crystal orientations. Geometrically, these areas are separated by straight lines defined by composition planes of the twins (Ref 31). Apparently, the deformation and residual stress was not recovered, as opposed to the Al-based deposits.

The detail of a reinforcement particle and its interface with the surrounding matrix is shown in Fig. 5. The diamond core and the surrounding layers of the cladding are
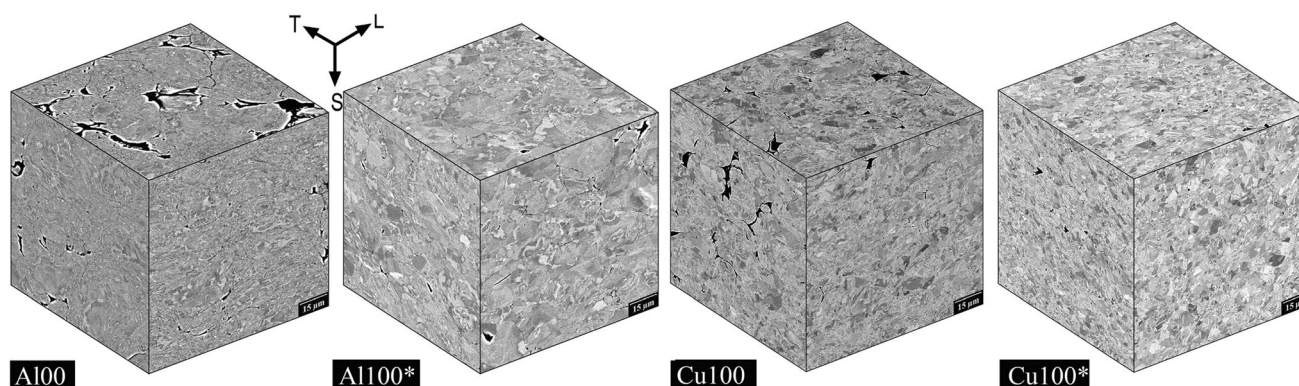

Fig. 2 Pseudo-3D microstructure of the pure metal deposits. SEM, backscattered electron contrast. Each cube edge is 100 μm
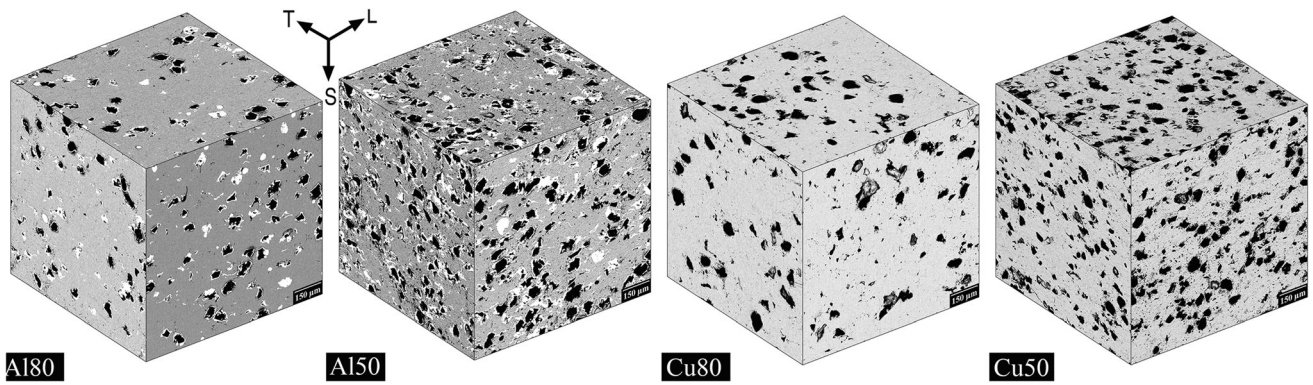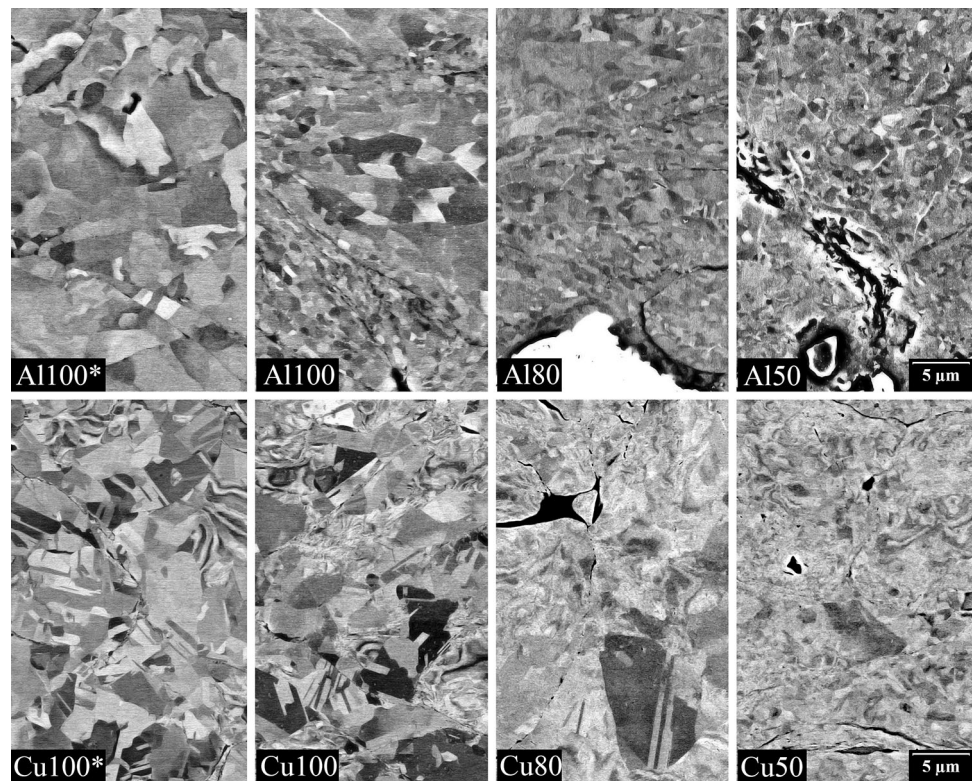
Fig. 3 Pseudo-3D microstructure of the investigated DMMC. SEM, backscattered electron contrast. Each cube edge is 1 mm

Fig. 4 Microstructure of the matrix in the investigated deposits. SEM, ECCI contrast

apparent for both DMMC types. While the cladding was virtually intact in the Al-based DMMC, the Cu-based DMMC frequently showed marked discontinuities at the cladding–matrix interface. Often, the cladding was missing in significant part of the interface, see Fig. 5. The separation of the cladding was probably caused by high stiffness of the Cu matrix and a resulting higher impact stress. The mechanism forming these discontinuities originates from the fact that the reinforcement particle deforms significantly less at impact when compared to the matrix particles. As a result, the just-deposited diamond particles will stick out of the deposit surface, forming a local surface

roughness. The flattening of subsequently deposited matrix particles is limited by this local roughness and the discontinuity is formed. The softer Al matrix adapts to the reinforcement more easily and less porosity was therefore found around the reinforcement particles, indicating better particle–matrix contact (see Fig. 5). On the other hand, the cladding was often damaged during impact of the reinforcement particles into the stiffer Cu matrix, creating localized debris areas around the reinforcement. These debris areas further promoted imperfect bonding and porosity formation around the reinforcement particles, decreasing the matrix–particle contact quality.

Fig. 5 Matrix–reinforcement interfaces, SEM, ECCI contrast. Note the marked discontinuity at the cladding–Cu matrix interface which was a frequently observed phenomenon. Also illustrated here is a missing cladding at bottom of the particle in the same DMMC type
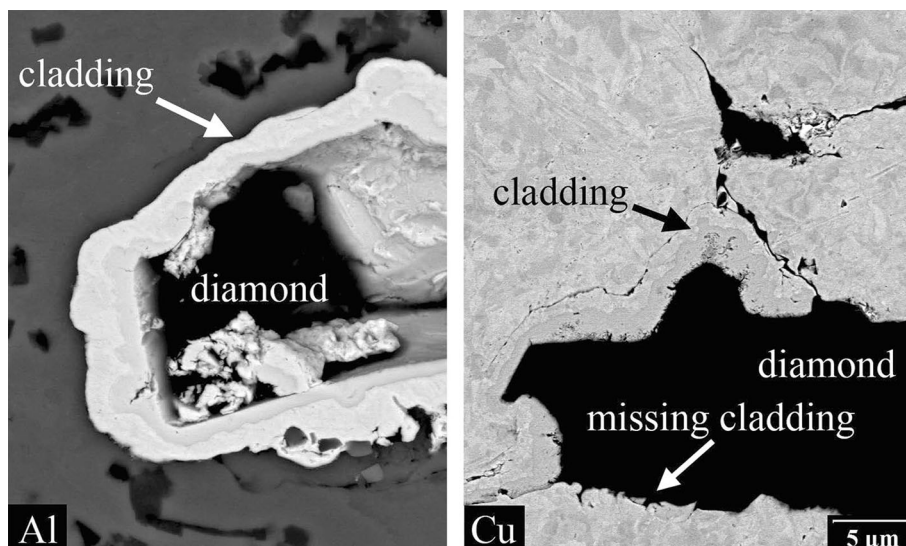

Table 3 Mechanical properties of the investigated cold-sprayed DMMC. Asterisks denote reference samples from [15]. Suffixes c and t denote compression and tension. The ρ/ρ_b values in parentheses are referenced to bulk rolled matrix material

Deposit type	Density			RUS		4PB stress–strain						Fracture mechanics	
	ρ (g/cm^3)	ρ/ρ_b (%)	c_r (vol.%/ wt.%)	E_S (GPa)	E_{LT} (GPa)	E (GPa)	E_t (GPa)	E_c (GPa)	$R_{p0.2t}$ (MPa)	$R_{p0.2c}$ (MPa)	R_{mt} (MPa)	K_{IC} (MPa·m$^{0.5}$)	$K_{th,eff}$ (MPa·m$^{0.5}$)
Al100[*]	2.66	98.5		66.9	66.6	71	75	69	69	70	>89	10.8 ± 1.6	1.4
Al100	2.51	93.0		49.9	55.13	49	50	44			81	3.8 ± 0.3	1.8
Al80	2.85	(105.6)	14/24	70.3	72.2	67	48	78	135	187	147	7.2 ± 0.3	2.6
Al50	3.14	(116.3)	25/40	77.7	79.3	72	54	82	146	210	155	7.1 ± 0.9	2.9
Cu100[*]	8.85	98.8		120.7	122.3	110	100	113	343	.	348	8.7 ± 1.1	3
Cu100	8.34	93.1		98.6	98.5	91	79	100			120	5.6 ± 0.1	1.7
Cu80	7.91	(88.3)	13/23	99.8	105.5	88	57	96			106	6.8 ± 0.5	2
Cu50	7.18	(80.1)	35/52	89.2	102.7	87	62	94			92	6.0 ± 1.4	2.5

Density and Diamond Content

The density of cold spray coatings is a reliable indicator of their quality, in particular when related to reference bulk materials (ρ_b) using relative coating density ρ/ρ_b (Table 3). The relative density of the pure Al100 and Cu100 coatings was approximately 93%, i.e., somewhat lower than 99% for the reference coatings Al100[*] and Cu100[*], providing a basic benchmark of the pure metal deposit quality. Unfortunately, the theoretical bulk density for studied DMMC was not known with sufficient precision due to uncertainties in their composition. Instead, the relative density of DMMC is referenced to rolled bulk matrix materials in Table 3 and gives just another quantification of the influence of reinforcement-to-matrix ratio. The approximate density of particles with 1:1 cladding-to-

diamond mass ratio is about $\rho_r = 5.0$ g/cm^3 (Table 1). This is significantly higher than density of bulk Al ($\rho_b = 2.7$ g/cm^3) and the density of Al-based DMMC should therefore be higher than that of the pure Al deposit. Naturally, an opposite holds for the heavier Cu matrix ($\rho_b = 8.96$ g/cm^3). Both trends can be clearly observed in Table 3. The absolute density values in Table 3 can also be used to estimate the reinforcement volumetric concentrations c_r, as $c_r = \frac{\rho - \rho_m}{\rho_r - \rho_m}$, and convert it to mass concentration subsequently. Here, ρ_r is the density of a clad diamond particle and ρ_m corresponds to the density of the matrix approximated by the density of pure metal deposits Al100 or Cu100. The computed reinforcement particle volumetric concentrations qualitatively correspond to the microstructure observations shown in Fig. 3. Moreover, the estimated mass concentration (see Table 3) corresponds to feedstock

powder composition and thus shows that both matrix and reinforcement deposited with similar deposition efficiency. Note that the volumetric concentrations include the diamond–cladding and the volume of the pure diamonds represents about 70% of the clad particle.

Stress–Strain Properties

The stress–strain behavior is an important quality that predetermines the practical use of any engineering material. The tensile and compression stress–strain curves computed from the four-point bending tests are presented in Fig. 6. Both investigated pure metal coatings showed brittle behavior in tension with fracture strain below 0.2%. The compression and tension curves of these specimens were similar, mainly because they broke in the elastic regime, i.e., before any significant difference could be observed. The engineering characteristics of the stress–strain curves are summarized in Table 3. Tensile and compressive moduli E_t and E_c of the deposits were evaluated, as well as a standard symmetrical bending modulus E describing a material with equal moduli in both tension and compression. Other presented properties are the ultimate tensile strength R_{mt} and yield strength $R_{p0.2t}$. Compared to their pure metal counterparts, the values of compressive and tensile moduli of the DMMC provide important information concerning the reinforcement particle-matrix contact. The presence of the reinforcement particles which are much stiffer than the matrix (for the elastic modulus of all involved materials, see Table 1) should significantly increase the coating modulus in both tension and compression (see (Ref 32) for relevant models). At the same time, any imperfect contact or even porosity at the diamond–cladding or cladding–matrix interfaces may decrease it as shown in (Ref 33). Along with the modulus change of the matrix, these two conflicting factors determine the elastic modulus of the DMMC. When compared to pure metal coating Al100, the Al-based

DMMC showed a compression moduli E_c higher by about 80% and comparable E_t moduli in tension (see Table 3). This indicates that, in compression, the stiffness effect of the reinforcement together with the matrix modulus increase was stronger than the detrimental interface effect. In tension, the effects equilibrated when the reinforcement–matrix interface areas detached. In the Cu-based DMMC, the ratio $\frac{E_{reinforcement}}{E_{matrix}}$ is lower than in the Al-based ones due to the higher modulus of the Cu matrix. Therefore, for Cu, a lower contribution of the particles to the overall DMMC stiffness can be expected. In compression, this (reduced) stiffness effect, along with the matrix modulus increase, was counteracted by the interface effects (stronger than for Al, in accordance with the splat interface observations presented in Fig. 5). As a result, no effect of reinforcement on compression modulus was observed. In tension, the negative effect was even more pronounced when the reinforcement–matrix interfaces detached and the overall tension modulus decreased by about 25%. Finally, the presence of diamonds increased the rupture strain of both Al- and Cu-based DMMC, indicating a higher ductility of the matrix.

In order to verify the partially unexpected results of bending tests, resonance ultrasound spectroscopy analysis was carried out. The elastic moduli characterizing a transversely isotropic material are presented in Table 3: out-of-plane values E_S of modulus in the direction parallel to spray direction (S axis in Fig. 1) and the in-plane values E_{LT} (in L-T plane in Fig. 1). RUS is a tension–compression method at low loads where an identical tension and compression stiffness is assumed. Similarly, if an identical assumption is made, a symmetrical modulus E can be computed from the bending test data. The symmetrical bending modulus E can then be compared with the RUS modulus E_{LT} that is measured in the same plane. The values of RUS moduli E_{LT} were about 20% higher than the symmetrical moduli E from bending. This difference can be explained by the behavior of inter-splat interfaces,

Fig. 6 Stress–strain properties of Al- and Cu-based cold-sprayed DMMC deposits. Reference high-pressure cold spray deposits are denoted by asterisks
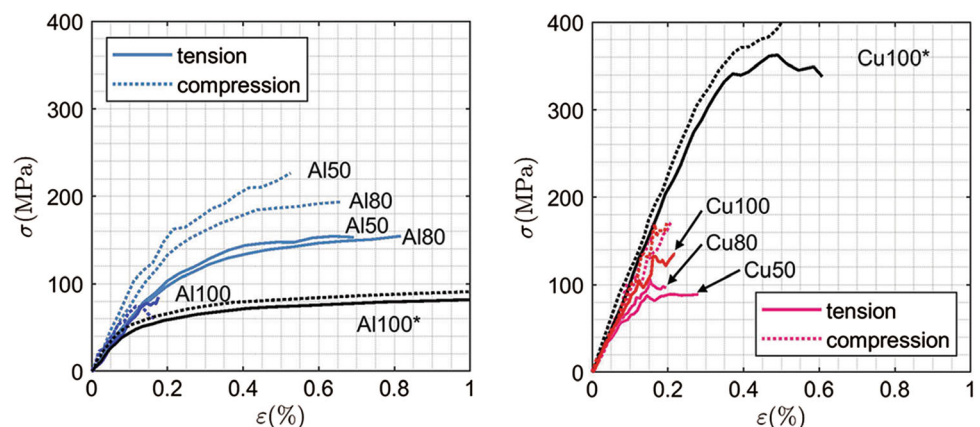
which likely remained closed during the low-load RUS testing, but detached during the bending. At the same time, the trends in the difference between the DMMC and the pure coatings were similar and the RUS results therefore confirmed the observations from the bending test.

Notably, the RUS analysis showed only small differences between the out-of-plane E_S and the, slightly higher, in-plane E_{LT} moduli. The observed lower out-of-plane moduli E_S indicated that a higher proportion of the inter-splat interfaces are situated within the L-T plane. Nevertheless, the differences in the two moduli accounted for less than 5%, indicating a good global isotropy of the materials. The only exceptions were pure metal deposit Al100 and Cu50 DMMC, where the anisotropy reached about 10%.

Fatigue Crack Growth Rate

Fatigue crack growth rate of cold-sprayed DMMC is crucial for engineering applications as these materials inherently contain defects such as cracks, pores and interfaces that may all act as fatigue crack initiators. The growth of the fatigue cracks is described by a relation of the crack growth rate da/dN to a suitably selected crack-driving force, such as the maximum value of the stress intensity factor encountered during a loading cycle (K_{max}) or its effective range ΔK_{eff} (the range when the crack can be considered open). The relations of the crack growth rate da/dN to these two crack-driving forces are plotted in Figs. 7 and 8. The observed differences between K_{max} and ΔK_{eff} are typical for the used loading type (similar differences were observed for cold-sprayed pure metals in (Ref 19)). At low crack growth rates, the ΔK_{eff} of the cold-sprayed deposits was lower than K_{max}. This can be caused by the roughness-induced crack closure, irreversible splat sliding or residual stress. At higher crack growth rates encountered at higher crack lengths, both the remaining ligament and the crack faces deform irreversibly and together with increasing crack tip opening displacement

lead to the increase in the ΔK_{eff} range beyond the value of K_{max}.

The shape of da/dN vs. K curves differed significantly for the Al- and Cu-based deposits. The Al-based deposits showed very steep crack growth curves near the threshold, with an elbow at da/d$N \sim 10^{-8}$ m/cycle. Below the elbow, some oscillations in the K direction can be observed. These oscillations are stronger in the ΔK_{eff}-based plot than in the K_{max}-based one. It is unclear whether this is an effect of the loading history or an artifact of the remote ΔK_{eff} measurement. As a result of the diamond presence, both observed crack-driving forces K_{max} and K_{eff} increased over the whole tested da/dN range by a factor of $\sim 1.5\times$. This contrasts somehow with the observed behavior of powder metallurgy MMC, where a significant plasticity of the matrix is usually observed. For example, the da/d$N(\Delta K)$ curves of SiC-reinforced Al–Zn–Mg–Cu matrix studied in (Ref 34) or Al_2O_3 particles-reinforced 6061 aluminum alloy matrix described in (Ref 35) showed increased resistance in the near-threshold region only, whereas the Paris region remained unaffected by the particles presence. On the other hand, the shift over a whole da/dN was observed in the da/d$N(\Delta K_{eff})$ plot in (Ref 34). The Cu-based deposits showed relatively straight crack growth rate curves down to 10^{-9} m/cycle, with a very indistinct near-threshold elbow at lower crack growth rates. Their da/d$N(K_{max})$ curves did not differ significantly and no systematic dependence on the diamond concentration was observed. However, the difference of da/d$N(\Delta K_{eff})$ curves in the near-threshold region was obvious as well as the dependence of da/d$N(\Delta K_{eff})$ on reinforcement particle concentration.

For both Cu and Al, the slopes of the linear part of the curves, i.e., the exponent n in the Paris law $\frac{da}{dN} = CK^n$ are relatively high, in the range from 7 for Al and even higher, at around 10 for Cu. This correlates with the fact that static mechanisms such as particle decohesion are active and contribute to the fatigue failure process in this load range, as will be shown later by the fractographic analysis.

Fig. 7 Crack growth rate da/dN as a function of K_{max}. Solid lines denote reference values taken from [19], black line represents the baseline data of a cold-rolled sheet, reference high-pressure cold spray deposits are denoted by asterisks
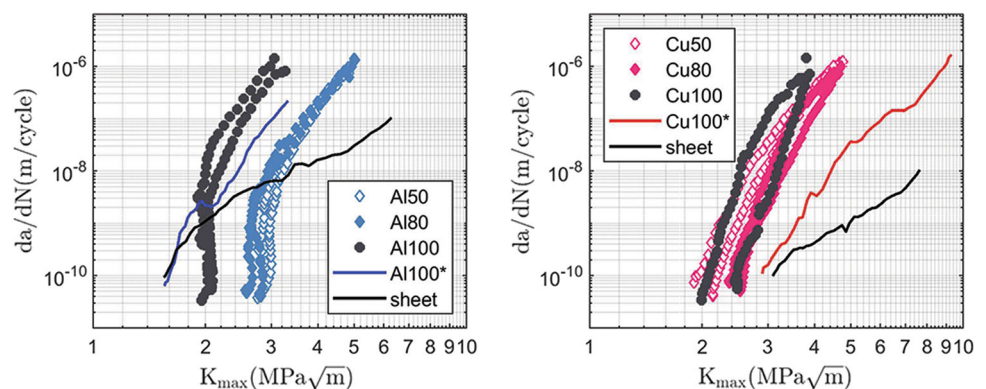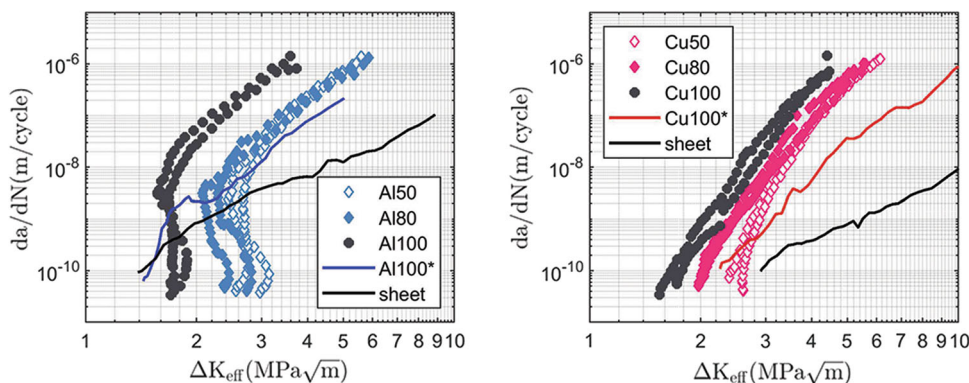
Fig. 8 Crack growth rate da/dN as a function of effective stress intensity factor $\Delta K_{\rm eff}$. Solid lines denote reference values taken from [19], black line represents the baseline data of a cold-rolled sheet, reference high-pressure cold spray deposits are denoted by asterisks

Fracture Toughness

Fracture toughness describes a material's resistance against static crack extension and enables to estimate its loading capacity when cracks or other sharp, stress-concentrating defects are present. The crack growth resistance curves obtained for the investigated materials are presented in Fig. 9. These curves relate J-integral, i.e., the elastic energy release rate caused by a growing crack (i.e., energy released by a unit area of a newly formed crack), to the actual crack extension Δa from the original fatigue pre-crack. Resistance curves increasing with crack extension Δa were observed for all deposit types. The values of fracture toughness $K_{\rm IC}$, i.e., values of stress intensity factors at the beginning of crack growth derived from the R-curves, are provided in Table 3. The toughness values of pure metal deposits are lower than the corresponding reference deposits Al100* and Cu100*. The presence of reinforcement leads to a higher $K_{\rm IC}$ in both Al- and Cu-based DMMC, with the effect more pronounced in the Al-based coatings. The fracture toughness of DMMC was, however, still lower than that of the reference deposits.

X-ray Diffraction

XRD was used to indirectly characterize the matrix material by means of coherently diffracting domain size $d_{\rm CDD}$

and residual stress magnitude $\varphi_{\rm residual}$. The measured $d_{\rm CDD}$ was very small, characterizing rather the size of dislocation cells or other sub-structural elements far smaller than the actual grain size and, as such, it could not be safely used to observe the effect of dynamic recrystallization. Still, it can provide a rough measure of thermally induced material grain growth and recovery. The measured values of $d_{\rm CDD}$ for the feedstock powder and all investigated coatings are included in Table 4. For the investigated Al-based coatings, the feedstock featured a relatively coarse substructure with $d_{\rm CDD} = 368$ nm. The investigated deposits had significantly lower $d_{\rm CDD}$, in the range 139-198 nm.

This decrease is possibly caused by micro-stress or substructure refinement (see (Ref 36)), both of these being indicators of dynamic recrystallization. The $d_{\rm CDD}$ of Cu-based deposits was compared to (Ref 37). For the investigated Cu-based coatings, the $d_{\rm CDD}$ always decreased with the change from the feedstock powder to the deposit, indicating dynamic recrystallization with the $d_{\rm CDD}$ comparable to cold worked Cu observed in (Ref 37) and a limited recovery. The observed comparable $d_{\rm CDD}$ of reference powder and deposit Cu100* can be explained by dynamic recrystallization followed by more significant recovery than in the case of investigated Cu-based deposits. Still, the $d_{\rm CDD}$ of the reference deposits did not reach the values of annealed Cu from (Ref 37) ($d_{\rm CDD} \sim 100$ nm) possibly indicating incomplete annealing.

Fig. 9 R-curves of the Al- and Cu-based cold-sprayed DMMC. Pre-crack length ~ 1.8 mm. The dotted line is the arbitrary construction line of ASTM E1820 standard. The symbols with center dots define the values of respective fracture toughness, reference high-pressure cold spray deposits are denoted by asterisks
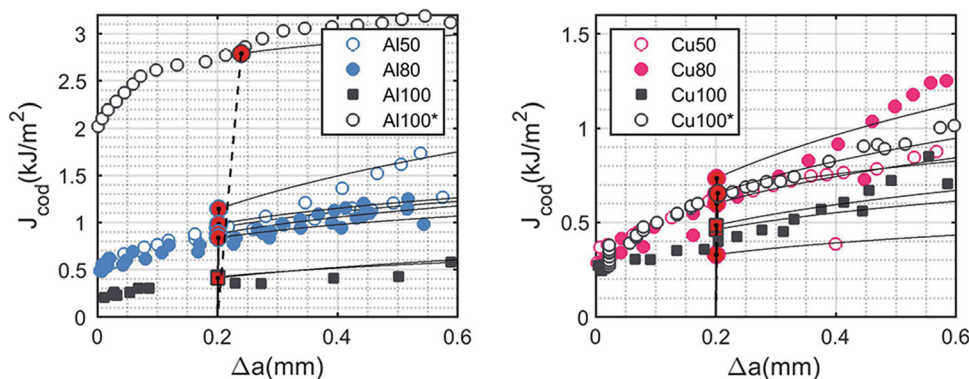
Table 4 Results of XRD and instrumented indentation (suffix IT) measurements of deposit matrices and feedstock powders. The value of residual stress σ_{residual} and the size of coherently diffracting domain d_{CDD} are included

Material	E_{IT} (GPa)	HV$_{\text{IT}}$ [-]	σ_{residual}(MPa)	d_{CDD} (nm)
Al powder*				200
Al powder				368
Al100*	71.7 ± 4.3	37.6 ± 2.2	–15 ± 3	369
Al100	64.4 ± 7.4	55.8 ± 8.2	–1 ± 2	153
Al80	77.4 ± 4.8	61.7 ± 5.3	–18 ± 2	139
Al50	76.9 ± 5.7	63.9 ± 5.4	–23 ± 3	198
Cu powder*				63
Cu powder				70
Cu100*	125.1 ± 8.1	134.7 ± 4.3	–103 ± 5	56
Cu100	111.5 ± 5.5	116.8 ± 13.6	–43 ± 3	20
Cu80	120.6 ± 5.5	132.8 ± 11.5	–67 ± 4	30
Cu50	118.4 ± 12	130.6 ± 14.9	–58 ± 8	32

The residual stress in the matrix of deposits is shown in Table 4. The small presented error values indicate that the lattice spacing conforms to the assumptions of the $\sin^2\psi$ method and indicate the measurement uncertainty in the probed area. In the pure metal deposits, the nonzero $\varphi_{\text{residual}}$ indicates that the method does not probe all regions equally and is actually biased toward compressive stress, which may form inside the splat's interior in response to the compressive plastic deformation at the interfacial area. In this case, the measured residual stress may be regarded as an indication of the severity of interfacial plastic deformation and the impact stress. Indeed, the high-pressure deposits Al100* and Cu100* where a higher impact intensity could be expected showed significantly higher residual stress magnitude than the coatings Al100 and Cu100, by a factor of 13× and 2.4×, respectively. In other words, the residual stress magnitude is related to the impact stress, which causes a formation of compressive residual stress inside the splats.

The relatively low residual stresses found in the Al-based coatings suggest that the residual stress was released by the recovery process. In contrast, the Cu matrix deposits retained significant residual stress. The effect of diamond addition on the residual stress is apparent for both matrix types. The matrix in all diamond-containing deposits shows higher magnitude of compressive stress than in the pure metal deposits. On the other hand, it seems that there is no clear trend between the actual diamond concentration and residual stress.

Microhardness and Indentation Modulus of Matrix

Instrumented micro-indentation represents an efficient method for measuring local mechanical properties of a particular phase in a material. The measured instrumented microhardness H_{IT} and indentation modulus E_{IT} of the matrix results are presented in Table 4. The interacting volume for hardness measurement is defined by the indent diagonal. In our case, the load was selected to 0.5 N, resulting in diagonals around 40–50 μm for the Al-based deposits and 25–30 μm for the Cu-based ones. That said and considering the splat dimensions, only a very limited influence of the diamond stiffness can be expected and the measurements should provide a reliable matrix characterization. The validity of this assumption is supported by the fact that the values of H_{IT} and E_{IT} are virtually identical for both DMMC types, regardless of the actual reinforcement concentration.

The investigated pure metal deposits showed lower E_{IT} modulus by about 12% compared to the high-pressure Al100* and Cu100*. The microhardness H_{IT} decreased by a similar factor for Cu. The reference Al100* deposit, however, showed much lower H_{IT}, as a result of bigger grain size (see Fig. 4) through the material recovery. From the investigated deposits, the pure Al deposit Al100 had the lowest indentation modulus and hardness, while the Al-based DMMC showed an increase by 13 and 20% in H_{IT} and E_{IT}. For the investigated Cu-based DMMC deposits, E_{IT} and H_{IT} were higher by 8 and 12% when compared to the Cu100 deposit. In summary, the DMMC showed a harder and stiffer matrix than the corresponding pure metal deposits, indicating improved properties. This improvement shows similar saturation behavior as the residual stress, i.e., it does not increase with diamond concentration.

Fractography

Fractography represents an effective method for the description of both static and fatigue failure mechanisms. The observed micromorphology of the fracture surfaces is shown in low magnification in Fig. 10 and in detail in Fig. 11 for slowly growing fatigue cracks (da/d$N \sim 10^{-9}$ m/cycle) and in Fig. 12 for a static fracture generated

Fig. 10 Fatigue fracture surface of cold-sprayed deposits fractured at da/dN = 10^{-9} m/cycle. SEM micrograph, backscattered electrons, shadow mode. Crack grows from the bottom to the top
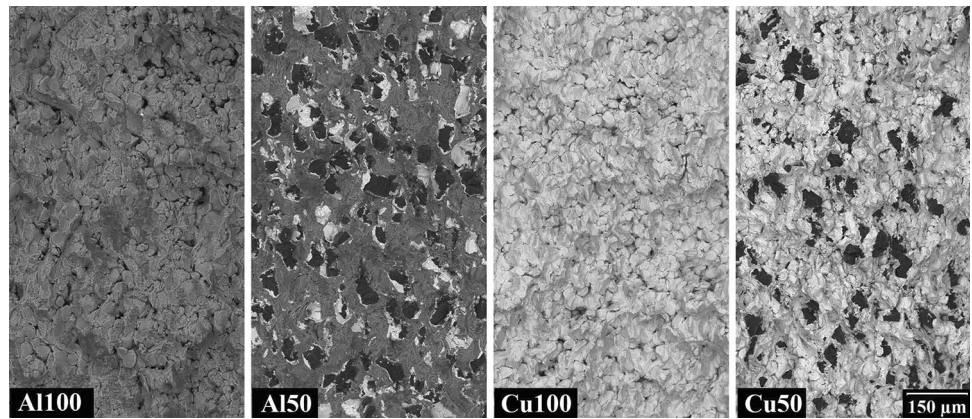

Fig. 11 Details of fracture surface of cold-sprayed deposits fractured at da/dN = 10^{-9} m/cycle. Arrows show signs of trans-splat fatigue cracking. SEM micrograph, backscattered electrons, shadow mode
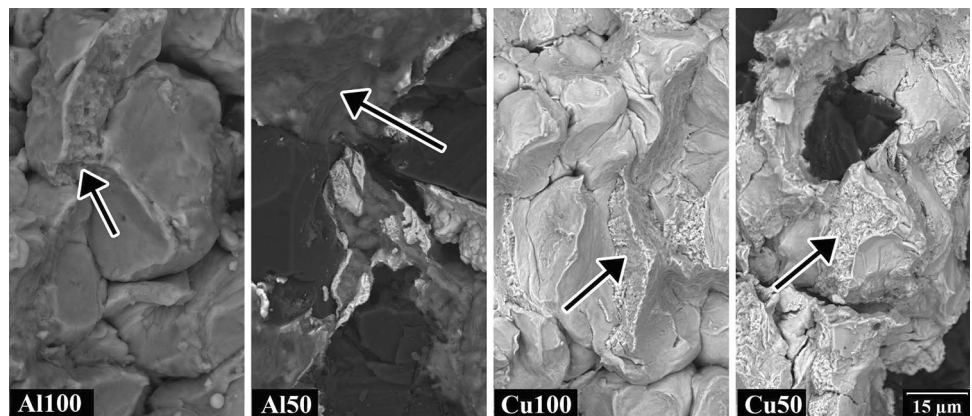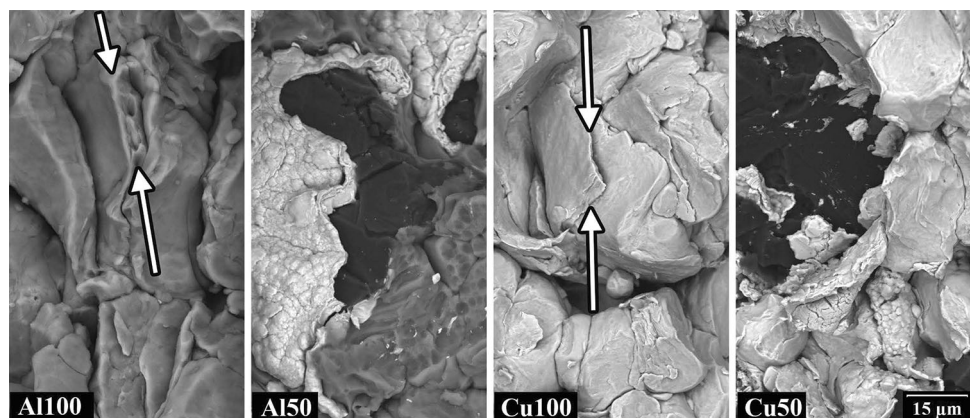

Fig. 12 Details of fracture surface of cold-sprayed deposits fractured in a static mode in the fracture toughness test. Arrows show trans-particle fracture with signs of plasticity. SEM micrograph, backscattered electrons, shadow mode

during the fracture toughness test. The fracture of the matrix took place by the combination of inter-splat decohesion and a trans-splat crack growth. The trans-splat cracking was observed in the near-threshold fatigue region of all deposits (see Fig. 11). In fact, it was a dominant near-threshold mechanism for the Al-based DMMC, where the complete matrix fracture was formed by trans-splat cracking, but contributed only partially to crack propagation in the other deposits. Contrary to this, the Paris regime of all deposits was dominated by inter-splat decohesion with no trans-splat crack growth observed. The static

failure of all deposits was also dominated by inter-splat decohesion but showed also a very limited amount of ductile trans-splat failure, see arrows in Fig. 12.

Characterization of the failure mode of the reinforcement particles was more difficult and required their analysis on both opposing fracture faces. For the Al-based deposits, three image intensities corresponding to the Al matrix, the Cu-Ni cladding and the diamond cores could be observed (Fig. 13). This enabled to determine the type of fracture of individual reinforcement particles as cladding–matrix (55.4% of particles by number), cladding–diamond
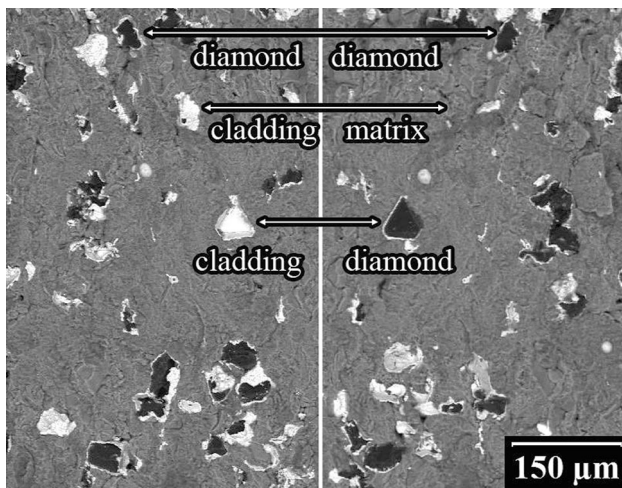
Fig. 13 Matching fracture surfaces of Al80 DMMC, illustrating three types of the reinforcement fracture. Note the trans-splat failure of the Al matrix

(40.8%) and diamond–diamond (3.8%). For the Cu-based deposits, it was impossible to differentiate the cladding from matrix (both copper), thus cladding–matrix fracture could not be detected. If we assume the same ratio of cladding–diamond to cladding–matrix fracture types as in case of the Al-based deposits, the resulting fracture type proportion will be similar to Al: cladding–matrix 54.9%, cladding–diamond 42% and diamond–diamond 3.1%. In other words, the diamond–diamond fracture was very rare, which corresponds to (Ref 10), where the diamond–cladding interface is denoted as the weakest point of the composite. No correlation of the individual diamond fracture modes with their concentration or type of loading was found.

Summary

The obtained results provided experimental evidence of the effects of the two suggested mechanisms shaping the mechanical and fracture properties of the investigated DMMC: changes in the matrix properties and loading stress redistribution into the reinforcement particles. At the same, the microstructural and fractographic observations enabled to form hypotheses regarding their origin.

The matrix properties were clearly influenced by the presence of the reinforcement particles as the matrices in the DMMC showed residual stress, microhardness and indentation modulus higher than those in the pure metal deposits. Increasing the impact stress either by using higher spray parameters (Table 2) as in the case of the high-pressure reference specimens or by impact of stiff diamond particles as in the case of DMMC leads to the increase in residual stress (see Table 4 and Sect. 3.6). The increased

indentation modulus and hardness (see Table 4 and Sect. 3.7) of the matrix in DMMC is also an indication of increasing the quality of inter-splat interfaces and can also be attributed to peening by higher impact stresses. The above effects were present in both Al and Cu matrices, regardless of the actual particle-to-matrix density ratio (which is around 2 for Al matrix and around 0.6 for Cu-based matrix when values in Tables 1 and 3 are used). Therefore, it is suggested here that this tamping/peening effect (see the review (Ref 32)) is connected to the stiffness of the reinforcement particle rather than to its weight. For the clad diamonds used in our study, the stiffness of the reinforcement is much higher than the stiffness of both matrices, approximately $10\times$ for Al matrix and around $6\times$ for Cu matrix, assuming a rule of mixtures for the double-clad particles and using values from Table 1. Obviously, an impact of a stiffer particle would invoke higher impact stress and this effect will be more amplified for Al as a more compliant matrix. Not surprisingly, the increase in indentation properties is higher in the Al-based DMMC (20 and 13% increase in E_{IT} and H_{IT} compared to Al100) than in the Cu-based ones (8 and 13% increase in E_{IT} and H_{IT} compared to Cu100), see Table 3. In summary, the matrices of DMMC exhibited enhanced properties compared to pure metals and the improvement was more prominent in the case of Al. An interesting finding is the long range of reinforcement particle impact influence witnessed by the instrumented indentation as the indent distance from nearest reinforcement particle was several tens to actually hundreds of micrometers.

The effect of the reinforcement particles on stress redistribution is predetermined by their stiffness and the quality of the reinforcement–matrix interface. For the investigated DMMC, reinforcement particles possessed a significantly higher stiffness than the matrix, thus they should, in theory, carry a significant part of the imposed load both in tension and compression. For both loading types, however, the reinforcement effect is moderated by the compliance of the reinforcement–matrix interface. This compliance lowers the overall modulus of the MMC as noted in (Ref 38). It arises from the discontinuities formed around the reinforcement particle observed in Fig. 5. Apart from the reinforcement–matrix interface compliance, the reinforcement–matrix bonding strength also comes into play when tension loading is considered and compliance is increased as soon as the particle debonds. The effect of the above described properties of reinforcement–matrix interfaces predetermines the tensile and compression moduli difference between the DMMC and the corresponding pure metal deposits. Despite the higher observed local matrix indentation modulus, the tensile modulus of all investigated DMMC was lower or comparable to the corresponding pure metals. Such result suggests that the combination of

relatively lower bonding strength and high compliance reinforcement–matrix interface prevented the stress redistribution into reinforcement. With regard to compression, the Al-based DMMC showed a modulus higher than corresponding pure metal deposit, indicating sufficient reinforcement–matrix interface stiffness was achieved in the process. For Cu-based DMMC, the compressive elastic modulus was slightly lower than the pure metal deposits, despite the increase in the modulus of the matrix. That said, the effect of the increased reinforcement particle stiffness was negated by porosity-induced decrease in reinforcement–matrix interface stiffness.

In summary, the stress redistribution into reinforcement particles was limited by the reinforcement–matrix interface compliance and partially decreased bonding strength. This limitation is more important for properties where the specimen is loaded predominantly in tension, such as fracture toughness and, partially, the fatigue crack growth rate. Under such loading, the reinforcement particles lose their contact with the matrix and do not contribute to the global specimen stiffness. In other words, their effect will be similar to the effect of equally sized voids.

Conclusions

Complex mechanical characterization of cold-sprayed Al- and Cu-based DMMC revealed their improved properties compared to the pure metal deposits prepared by the same technology. In terms of values, the DMMC showed the following differences from the pure metal deposits:

- Improved coating strength (+86%), ductility (+200%), fatigue crack growth resistance (+40 to +60%) and fracture toughness (+88%) were observed for Al-based DMMC.
- Decrease in coating strength (−24 to −12%), increased ductility (+25 to +60%), fatigue crack growth resistance (+15 to +45%) and fracture toughness (+10 to +20%) were observed for Cu-based DMMC.

In the search for the mechanisms underlying the observed differences, the strengthening mechanisms typically encountered in traditional MMCs as well as effects associated with cold spray technology were examined. This was done by performing a study of the local DMMC matrix properties as well as by observing the failure mode of both matrix and reinforcement in various loading modes including fatigue. It was found that:

- The matrices in the DMMC had better properties than those in the pure metal deposits. A more prominent improvement was observed for Al-based DMMC. The cause of this improvement is most probably the tamping/peening effect of the reinforcement particles that yielded a better inter-splat bonding of the matrix material. The effect is present regardless of the actual reinforcement–matrix density ratio, which suggests that the reinforcement particle stiffness is more important than their actual mass.

- The stress redistribution into reinforcement particles was limited by the lower reinforcement–matrix bonding strength and also by porosity formed around reinforcement particles during their deposition, as evidenced by the differences in compression and tension stress–strain curves of the DMMC. As such, this effect could not contribute to improvement of most of the mechanical properties that are characterized by tensile loading of tested material. The stress redistribution effect was observed only for the compressive loading of Al-based DMMC, where the softer matrix better adhered to the reinforcement.

- The failure mechanism of the DMMC matrix was related to loading type and amplitude. Trans-splat fatigue fracture was observed in Al-based deposits at near-threshold fatigue loads and partially also in other deposits at the same loading range. At higher loads, particle decohesion was the main failure mode in the matrix in all investigated fatigue fractures as well as in the static fractures, making the micromorphology of the two fracture surfaces virtually identical.

- The failure mechanism of the reinforcement particles was mostly decohesion from the matrix. Only a very small amount, typically less than 4% of the diamond particles were fractured, indicating limited diamond fragmentation during deposition.

From all considered mechanisms shaping the DMMC properties, the matrix improvement seems to play the most important role. As evidenced by the performed matrix property characterization, a significant improvement of the mechanical properties of a cold-sprayed metal matrix can be achieved by the tamping/peening effect of the reinforcement particles. This improvement is apparent in matrix areas even at a significant distance from the reinforcement particles, suggesting a long range of the effect. Moreover, it appears that this improvement is related to higher impact stress caused by high stiffness of the reinforcement particles rather than their density.

References

1. S.V. Kidalov and F.M. Shakhov, Thermal Conductivity of Diamond Composites, *Materials*, 2009, **2**(4), p 2467–2495. https://doi.org/10.3390/MA2042467

2. S. Yin et al., Advanced Diamond-Reinforced Metal Matrix Composites via Cold Spray: Properties and Deposition Mechanism, *Compos. B Eng.*, 2017, **113**, p 44–54. https://doi.org/10.1016/j.compositesb.2017.01.009

3. A.M. Abyzov et al., Diamond-Tungsten Based Coating-Copper Composites with High Thermal Conductivity Produced by Pulse Plasma Sintering, *Mater. Des.*, 2015, **76**, p 97–109. https://doi.org/10.1016/j.matdes.2015.03.056

4. J. Li, H. Zhang, Y. Zhang, Z. Che and X. Wang, Microstructure and Thermal Conductivity of Cu/diamond Composites with Ti-coated Diamond Particles Produced by Gas Pressure Infiltration, *J. Alloy. Compd.*, 2015, **647**, p 941–946. https://doi.org/10.1016/j.jallcom.2015.06.062

5. K. Venkateswarlu et al., Abrasive Wear Behavior of Thermally Sprayed Diamond Reinforced Composite Coating Deposited with Both Oxy-acetylene and HVOF Techniques, *Wear*, 2009, **266**, p 995–1002. https://doi.org/10.1016/j.wear.2009.02.001

6. W.Z. Shao, V.V. Ivanov, L. Zhen, Y.S. Cui and Y. Wang, A Study on Graphitization of Diamond in Copper–Diamond Composite Materials, *Mater. Lett.*, 2004, **58**(1–2), p 146–149. https://doi.org/10.1016/S0167-577X(03)00433-6

7. I.A. Ibrahim, F.A. Mohamed and E.J. Lavernia, Particulate Reinforced Metal Matrix Composites—A Review, *J. Mater. Sci.*, 1991, **26**(5), p 1137–1156. https://doi.org/10.1007/BF00544448

8. H.J. Kim, D.H. Jung, J.H. Jang and C.H. Lee, Study on Metal/Diamond Binary Composite Coatings by Cold Spray, *Mater. Sci. Forum*, 2007, **534–536**, p 441–444. https://doi.org/10.4028/WWW.SCIENTIFIC.NET/MSF.534-536.441

9. Luzin, V. et al., in *Cold-Spray Coatings* (Springer International Publishing, 2017), pp. 451–480

10. S. Yin et al., Metallurgical Bonding Between Metal Matrix and Core-Shelled Reinforcements in Cold Sprayed Composite Coating, *Scripta Mater.*, 2020, **177**, p 49–53. https://doi.org/10.1016/j.scriptamat.2019.09.023

11. B.Y. Zong, F. Zhang, G. Wang and L. Zuo, Strengthening Mechanism of Load Sharing of Particulate Reinforcements in a Metal Matrix Composite, *J. Mater. Sci.*, 2007, **42**(12), p 4215–4226. https://doi.org/10.1007/S10853-006-0674-7/FIGURES/12

12. P.J. Withers, W.M. Stobbs and O.B. Pedersen, The Application of the Eshelby Method of Internal Stress Determination to Short Fibre Metal Matrix Composites, *Acta Metall.*, 1989, **37**(11), p 3061–3084. https://doi.org/10.1016/0001-6160(89)90341-6

13. T. Christman, A. Needleman and S. Suresh, An Experimental and Numerical Study of Deformation in Metal-Ceramic Composites, *Acta Metall.*, 1989, **37**(11), p 3029–3050. https://doi.org/10.1016/0001-6160(89)90339-8

14. N. Fan et al., A New Strategy for Strengthening Additively Manufactured Cold Spray Deposits Through In-process Densification, *Addit. Manuf.*, 2020, **36**, 101626. https://doi.org/10.1016/J.ADDMA.2020.101626

15. O. Kovarik, J. Siegl, J. Cizek, T. Chraska and J. Kondas, Fracture Toughness of Cold Sprayed Pure Metals, *J. Therm. Spray Technol.*, 2019, **29**, p 147–157. https://doi.org/10.1007/s11666-019-00956-z

16. A. Migliori, & J.L. Sarrao, *Resonant Ultrasound Spectroscopy*, (Willey)

17. P. Sedlák, H. Seiner, J. Zídek, M. Janovská and M. Landa, Determination of All 21 Independent Elastic Coefficients of Generally Anisotropic Solids by Resonant Ultrasound Spectroscopy: Benchmark Examples, *Exp. Mech.*, 2014, **54**, p 1073–1085. https://doi.org/10.1007/s11340-014-9862-6

18. H. Seiner et al., Application of Ultrasonic Methods to Determine Elastic Anisotropy of Polycrystalline Copper Processed by Equal-Channel Angular Pressing, *Acta Mater.*, 2010, **58**(1), p 235–247. https://doi.org/10.1016/J.ACTAMAT.2009.08.071

19. Cizek, J. et al., Measurement of Mechanical and Fatigue Properties Using Unified, Simple-Geometry Specimens: Cold Spray Additively Manufactured Pure Metals. *Surf. Coat. Technol.*, **412**, (2021). Doi:https://doi.org/10.1016/j.surfcoat.2021.126929.

20. H. Herbert, Ueber den Zusammenhang der Biegungselastizität des Gußeisens mit seiner Zug- und Druckelastizität, *Forschungsarbeiten auf dem Gebiete des Ingenieurwesens*, 1910 https://doi.org/10.1007/978-3-662-02218-4_2

21. J. Blaber, B. Adair and A. Antoniou, Ncorr: Open-Source 2D Digital Image Correlation Matlab Software, *Exp. Mech.*, 2015, **55**(6), p 1105–1122. https://doi.org/10.1007/s11340-015-0009-1

22. R.A. Mayville and I. Finnie, Uniaxial Stress–Strain Curves from a Bending Test, *Exp. Mech.*, 1982, **22**(6), p 197–201. https://doi.org/10.1007/BF02326357

23. O. Kovarik, A. Materna, J. Siegl, J. Cizek and J. Klecka, Fatigue Crack Growth in Plasma-Sprayed Refractory Materials, *J. Therm. Spray Technol.*, 2019, **28**(1–2), p 87–97. https://doi.org/10.1007/s11666-018-0790-3

24. Ľ. Ambriško and L. Pešek, Measurement of the Steady State Tearing in Thin Sheets Using the Contactless System, *Metall. Res. Technol*, 2020, **117**, p 310. https://doi.org/10.1051/metal/2020032

25. T.H. Becker, M. Mostafavi, R.B. Tait and T.J. Marrow, An Approach to Calculate the J-Integral by Digital Image Correlation Displacement Field Measurement, *Fatigue Fract. Eng. Mater. Struct.*, 2012, **35**(10), p 971–984. https://doi.org/10.1111/j.1460-2695.2012.01685.x

26. I. Jandejsek, L. Gajdoš, M. Šperl and D. Vavřík, Analysis of Standard Fracture Toughness Test Based on Digital Image Correlation Data, *Eng. Fract. Mech.*, 2017, **182**, p 607–620. https://doi.org/10.1016/j.engfracmech.2017.05.045

27. X. Song et al., Residual Stresses in Single Particle Splat of Metal Cold Spray Process—Numerical Simulation and Direct Measurement, *Mater. Lett.*, 2018, **230**, p 152–156. https://doi.org/10.1016/j.matlet.2018.07.117

28. Y. Zou et al., Dynamic Recrystallization in the Particle/Particle Interfacial Region of Cold-Sprayed Nickel Coating: Electron Backscatter Diffraction Characterization, *Scripta Mater.*, 2009, **61**(9), p 899–902. https://doi.org/10.1016/J.SCRIPTAMAT.2009.07.020

29. R.K. Roy, Recrystallization Behavior of Commercial Purity Aluminium Alloys, *Light Metal Alloys Appl.*, 2014 https://doi.org/10.5772/58385

30. G. Benchabane, Z. Boumerzoug, I. Thibon and T. Gloriant, Recrystallization of Pure Copper Investigated by Calorimetry and Microhardness, *Mater. Charact.*, 2008, **59**(10), p 1425–1428. https://doi.org/10.1016/J.MATCHAR.2008.01.002

31. B.D. Cullity, *Elements of X-ray Diffraction* (Addison-Wesley Publishing Company, Inc, Reading, 1978)

32. L. He and M. Hassani, A Review of the Mechanical and Tribological Behavior of Cold Spray Metal Matrix Composites, *J. Therm. Spray Technol.*, 2020, **29**, p 1565–1608. https://doi.org/10.1007/s11666-020-01091-w

33. L. Weng, Y. Shen, T. Fan and J. Xu, A Study of Interface Damage on Mechanical Properties of Particle-Reinforced Composites, *JOM*, 2015, **67**, p 1499–1504. https://doi.org/10.1007/s11837-015-1413-9

34. J.K. Shang and R.O. Ritchie, On the Particle-Size Dependence of Fatigue-Crack Propagation Thresholds in SiC-Particulate-Reinforced Aluminum-Alloy Composites: Role of Crack Closure and

Crack Trapping, *Acta Metall.*, 1989, **37**(8), p 2267–2278. https://doi.org/10.1016/0001-6160(89)90154-5

35. C. Li and F. Ellyin, On Crack Phases of Particulate-Reinforced Metal Matrix Composites, *Fatigue Fract. Eng. Mater. Struct.*, 1995, **18**(11), p 1299–1309. https://doi.org/10.1111/J.1460-2695.1995.TB00856.X

36. T. Ungár, G. Tichy, J. Gubicza and R.J. Hellmig, Correlation Between Subgrains and Coherently Scattering Domains, *Powder Diffr.*, 2005, **20**, p 366–375. https://doi.org/10.1154/1.2135313

37. S. Dey, N. Gayathri, M. Bhattacharya and P. Mukherjee, In Situ XRD Studies of the Process Dynamics During Annealing in Cold-Rolled Copper, *Metall. and Mater. Trans. A*, 2016, **47**, p 6281–6291. https://doi.org/10.1007/s11661-016-3768-0

38. S. Kumar, S.K. Reddy and S.V. Joshi, Microstructure and Performance of Cold Sprayed Al-SiC Composite Coatings with High Fraction of Particulates, *Surf. Coat. Technol.*, 2017, **318**, p 62–71. https://doi.org/10.1016/j.surfcoat.2016.11.047

39. C. Smithells, *Smithells Metals Reference Book*, Elsevier Butterworth-Heinemann, Amsterdam Boston, 2004.

40. S.F. Ferdous and A. Adnan, Mode-I Fracture Toughness Prediction of Diamond at the Nanoscale, *J. Nanomech. Micromech.*, 2017, **7**, p 04017010. https://doi.org/10.1061/(asce)nm.2153-5477.0000130

Publisher's Note Springer Nature remains neutral with regard to jurisdictional claims in published maps and institutional affiliations.